The Astrophysical Journal, 905:61 (14pp), 2020 December 10 https://doi.org/10.3847/1538-4357/abc42e

Star Formation and Evolution of Blister-type H II Region Sh2-112

Neelam Panwar[1], Saurabh Sharma[1], D. K. Ojha[2], T. Baug[3], L. K. Dewangan[4], B. C. Bhatt[5], and Rakesh Pandey[1]
[1] Aryabhatta Research Institute of Observational Sciences (ARIES), Nainital 263129, India
[2] Tata Institute of Fundamental Research, Mumbai (Bombay) 400005, India
[3] Kavli Institute for Astronomy and Astrophysics, Peking University, 5 Yiheyuan Road, Haidian District, Beijing 100871, People's Republic of China
[4] Physical Research Laboratory, Navrangpura, Ahmedabad 380009, India
[5] Indian Institute of Astrophysics, Koramangala, Bangalore 560034, India
Received 2020 August 13; revised 2020 October 8; accepted 2020 October 19; published 2020 December 14

Abstract

We report the observational findings of the Sh2-112 H II region by using the multiwavelength data analysis ranging from optical to radio wavelengths. This region is powered by the massive O8V-type star BD +45 3216. The surface density distribution and minimum spanning tree analyses of the young stellar object (YSO) candidates in the region reveal their groupings toward the western periphery of the H II region. A GMRT radio continuum emission peak is found toward the northwest boundary of the H II region and is investigated as a compact/ultracompact H II region candidate powered by a B0–B0.5-type star. Toward the southwest direction, a prominent curved rim-like structure is found in the Hα image and GMRT radio continuum maps, where the H_2 and ^{13}CO emission is also observed. These results suggest the existence of the ionized boundary layer (IBL) on the surface of the molecular cloud. This IBL is found to be overpressured with respect to the internal pressure of the surrounding molecular cloud. This implies that the shocks are propagating/propagated into the molecular cloud, and the young stars identified within it are likely triggered due to the massive star. It is also found that this region is ionization-bounded toward the west and density-bounded toward the east. Based on the distribution of the ionized gas, molecular material, and YSO candidates, we propose that the Sh2-112 H II region is a good candidate for the blister-type H II region that has been evolved on the surface of a cylindrical molecular cloud.

Unified Astronomy Thesaurus concepts: Star formation (1569); H II regions (694); Young stellar objects (1834)

Supporting material: machine-readable table

1. Introduction

Massive stars play dominant roles in the dynamical and chemical evolution of their host galaxies. Even in their short life span, they influence their surrounding environment through a large output of ultraviolet (UV) photons, strong stellar winds, outflows, and energetic supernova explosions (Zinnecker & Yorke 2007; Kruijssen et al. 2019). Massive stars create H II regions by ionizing the surrounding gas through their energetic radiation ($h\nu \geqslant 13.6$ eV). The interaction of the ionization/shock fronts from the expanding H II regions with the surrounding molecular material may trigger the formation of next-generation stars via various processes (see, e.g., Elmegreen 1998; Deharveng et al. 2005). In one of these processes, known as "collect and collapse," a dense shell of swept-up neutral material forms around the massive stars, becomes gravitationally unstable, and fragments to form new stars (Elmegreen & Lada 1977; Whitworth et al. 1994). The outcome of the above process is observed as the massive condensations or groups of young stars at the periphery (e.g., Deharveng et al. 2005; Zavagno et al. 2010). In another process, known as "radiation-driven implosion," ionization/shock fronts can compress the preexisting dense clumps and consequently induce the formation of new stars (Bertoldi 1989; Lefloch & Lazareff 1994). The surface of the dense clump may shield the remaining molecular cloud from the ionizing radiation, resulting in structures such as bright-rim clouds, globules, pillars, etc.

Though there are observational studies of a few star-forming regions (SFRs) investigating the influence of massive stars on their surroundings (see Pomarès et al. 2009; Zavagno et al. 2010; Baug et al. 2015; Panwar et al. 2017; Sharma et al. 2017; Dewangan et al. 2019; Panwar et al. 2019; Pandey et al. 2020, and references therein), the physical processes involved in the formation of massive stars and their interaction with the surrounding environment are observationally not very well established (Tan et al. 2014; Motte et al. 2018). The numerical simulations show that an expanding H II region will be able to trigger star formation if the ambient molecular material is dense enough (Hosokawa & Inutsuka 2006; Dale et al. 2007). However, observationally, it is not well studied, especially in the case of clumpy and inhomogeneous environments.

The Galactic H II region Sh2-112 ($\alpha_{2000} \sim 20^h33^m49^s$, $\delta_{2000} \sim +45°38'00''$) (Sharpless 1959) is powered by the massive star BD +45 3216 (Lahulla 1985; Hunter & Massey 1990). It is located toward one of the most active and massive star-forming complexes within 2 kpc distance in the Galaxy, Cygnus X, which is extended in an area of $\sim 7° \times 7°$ on the sky. Although once believed to be a superposition of many disconnected SFRs, Schneider et al. (2006) showed that the molecular clouds in Cygnus X form a coherent complex of nine OB associations at a similar distance of ~1.7 kpc. The entire complex exhibits evidence for many sites of star formation at different evolutionary stages, from the youngest embedded star formation in infrared (IR) dark clouds in DR21 (Downes & Rinehart 1966), to the young cluster Cygnus OB2 (Knödlseder 2000), to the more dispersed and perhaps older Cygnus OB9 region. The region Sh2-112 is associated with Cygnus OB6, adjacent to the North American and Pelican Nebula but at a farther distance (Uyanıker et al. 2001). Among all of the regions of Cygnus X, due to a complex morphology, Sh2-112 was a poorly studied H II region until now.

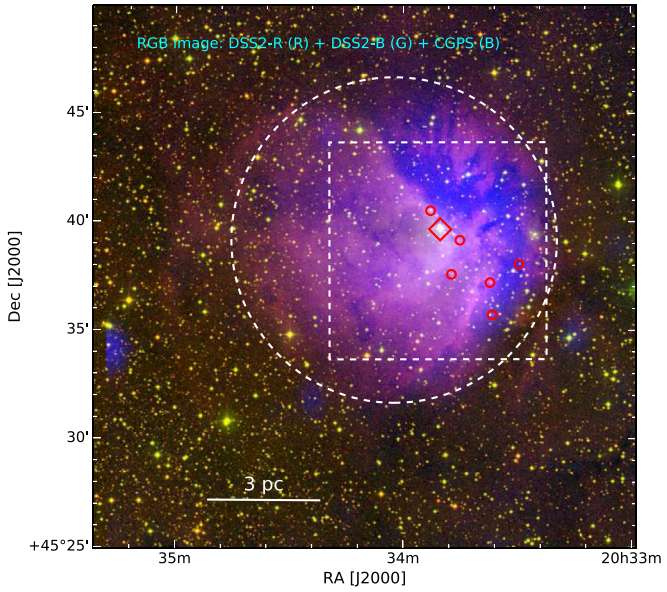

Figure 1. Color-composite image of the Sh2-112 region generated from the DSS2-R (red), DSS2-B (green), and CGPS 21 cm radio continuum (blue) images. The diamond represents the position of the ionizing star. The dashed circle shows the extension of the H II region (diameter ∼15′) in the optical images. Small red circles represent the Hα emission stars identified using slitless spectroscopy within the HCT FOV shown by the dashed box (10′ × 10′).

Figure 1 shows the color-composite view of the Sh2-112 region and reveals that the complex has a spherical shell-like morphology with a diameter of ∼15′. In addition to the observed interesting morphology, the complex is a relatively nearby star-forming site, making it a promising region to study the role of radiation feedback from massive star(s) in the evolution of the natal cloud. The distribution of the young stellar object (YSO) candidates helps us study the current sites of star formation and the relationships between high-mass stars and star formation activity in their parental molecular clouds. Determining how many low-mass stars form in clusters or relative isolation will improve our understanding of how low-mass stars form in molecular cloud complexes dominated by massive stars.

In the present work, we aim to identify and characterize the YSO candidates in the H II region and study the star formation history using multiwavelength data covering optical to radio wavelengths. Such an analysis offers an opportunity to examine the distribution of YSO candidates, dust temperature, column density, extinction, ionized emission, and molecular gas.

This paper is organized as follows. In Section 2, we present the multiwavelength observations of the Sh2-112 region and data reduction techniques. Other available archival data sets used in the present work are also summarized in Section 2. In Section 3, we present the optical spectrum of the brightest star and identification/characterization of YSO candidates. The morphology of the region inferred using multiwavelength observations followed by a discussion of the star formation scenario is presented in Section 4. In Section 5, the main conclusions of the present study are summarized.

2. Observations and Data Reduction

To understand the ongoing star formation processes in the Sh2-112 complex, we have utilized the available data starting from the optical to radio wavelengths. The details of these data are briefly described in the following subsections.

Table 1
Log of Optical Observations

Filter and Exposure (s) × No. of Frames	Date of Observations (Telescope)
[S II]: 300 × 1, Hα: 300 × 1, [O III]: 300 × 1	2010 October 12 (HCT)
U: 15 × 3, *B*: 5 × 2, *V*: 5 × 3, *I*: 1 × 2	2018 October 5 (DFOT)
Slitless Spectra	
Hα/gr 5: 300 × 2	2010 October 12 (HCT)
Slit Spectra	
BD +45 3216: 600 × 2	2010 October 12 (HCT)
Feige 15: 600 × 2	2010 October 12 (HCT)

2.1. Optical Observations

Optical [S II] (6724 Å), Hα (6563 Å), and [O III] (5007 Å) narrowband filter observations of the central region of the Sh2-112 H II region were carried out on 2010 October 12 using the Himalaya Faint Object Spectrograph and Camera (HFOSC) mounted on the 2 m Himalayan Chandra Telescope (HCT; for details, see Stalin et al. 2008; Chauhan et al. 2009). With an integration time of 300 s in each filter, the HCT observations cover a field of view (FOV) of ∼10′ × 10′. Along with the object frames, several bias and twilight flat-field frames were also obtained. The average seeing during the observations was ∼1″–1.″5.

We carried out the short-exposure optical (*UBVI*) observations of the Sh2-112 region (FOV ∼18′ × 18′) on 2018 October 5 using the 2k × 2k CCD camera mounted on the f/4 Cassegrain focus of the 1.3 m Devasthal Fast Optical Telescope (DFOT) of the Aryabhatta Research Institute of Observational Sciences (ARIES), Nainital, India (for details, see Panwar et al. 2017). The average seeing during the observing night was ∼2″. The log of observations is given in Table 1. Along with the object frames, several bias and flat frames were also taken during the same night. We also observed the Landolt standard stars' field (SA 92) on the same night. The standard field was used to calculate the extinction coefficients and calibrate our observations to the standard system.

Initial processing of the data frames (i.e., bias subtraction, flat-fielding, etc.) was done using the IRAF[6] data reduction package. The photometric measurements of the stars were performed using the *DAOPHOT − II* software package (Stetson 1987). The point-spread function (PSF) was obtained for each frame using several uncontaminated stars. Aperture photometry was carried out for the standard stars to estimate the atmospheric extinction and calibrate the observations. We found the value of the extinction coefficients in the *U*, *B*, *V*, and *I* filters to be 0.50, 0.26, 0.17, and 0.09, respectively. The following transformation equations were used to calibrate the observations:

$$(U-B) = (1.00 \pm 0.02)(u-b) + (-1.54 \pm 0.02),$$
$$(B-V) = (1.22 \pm 0.02)(b-v) + (-0.86 \pm 0.02),$$
$$(V-I) = (0.94 \pm 0.02)(v-i) + (0.20 \pm 0.01),$$
$$B = b + (0.07 \pm 0.02)(u-b) + (-2.90 \pm 0.02),$$
$$V = v + (-0.11 \pm 0.02)(v-i) + (-2.22 \pm 0.02),$$

[6] IRAF is distributed by the National Optical Astronomy Observatories, USA.

where u, b, v, and i are the instrumental magnitudes corrected for the atmospheric extinctions, and U, B, V, and I are the standard magnitudes.

The standard deviations of the standardization residual, Δ, between the standard and transformed V magnitude and the $(U-B)$, $(B-V)$, and $(V-I)$ colors of standard stars are 0.01, 0.02, 0.02, and 0.02 mag, respectively. We have used only those stars for further analyses that have a photometric uncertainty of <0.1 mag.

2.2. Optical Slitless Spectroscopy

We performed Hα slitless spectroscopic observations of Sh2-112 using the HFOSC on the 2 m HCT on 2010 October 12. The spectra were obtained with the combination of a wide Hα filter (6300–6740 Å) and grism 5 (5200–10300 Å) with a spectral resolution of 870 Å. The average seeing during the observations was $\sim 1\farcs2$. Two frames of slitless spectra, each with an exposure time of 300 s, were obtained and coadded to increase the signal-to-noise ratio (S/N) of the observed spectra. Emission-line stars were visually identified as an enhancement of Hα emission above the continuum. The six sources identified as emission-line stars within the HCT FOV are shown with red circles in Figure 1.

2.3. Optical Slit Spectroscopy

To ascertain the spectral type of the brightest star, BD +45 3216 (α_{2000}: $20^{\rm h}33^{\rm m}50\fs4$, δ_{2000}: $45°39'41''$), in the field, we obtained the spectrum using HFOSC with the help of grism 7 (3500–7000 Å), which has a resolving power of 1200 and a spectral dispersion of 1.45 Å pixel^{-1}. The spectrum of BD +45 3216 with an exposure time of 600 s was taken on 2010 October 12. In addition to an FeAr lamp arc spectrum (for wavelength calibration), multiple bias frames were also obtained. The spectrophotometric standard star Feige 15 (α_{2000}: $01^{\rm h}49^{\rm m}09\fs4$, δ_{2000}: $+13°33'12''$; Stone 1977) was also observed with an exposure time of 600 s. We reduced all of the spectra using the APALL task in the IRAF data reduction package. Finally, the flux-calibrated normalized spectrum of the bright star was obtained (see Figure 2).

2.4. Radio Continuum Observations

Radio continuum observations of the Sh2-112 region at the 610 and 1280 MHz bands were carried out using the Giant Metrewave Radio Telescope (GMRT) on 2010 October 22 (project code 19_026; PI: S. S. Borgaonkar) and 2012 November 9 (project code 23_019; PI: K. K. Mallick), respectively. Total observing time at the 610 and 1280 MHz bands was 5.4 and 4.5 hr, respectively. The Astronomical Image Processing Software (AIPS) package was used following the procedure described in Mallick et al. (2013). Various AIPS tasks were used to edit the data and flag out the bad baselines or time ranges. Additionally, the data quality was improved by multiple iterations of flagging and calibration. A few iterations of (phase) self-calibration were carried out to remove the ionospheric phase distortion effects. Finally, the data were Fourier-inverted to make the radio maps. The final 610 MHz image has a synthesized beam size of $60'' \times 60''$ and an rms of 48 mJy beam^{-1}. The final rms of the 1280 MHz image is about 0.13 mJy beam^{-1}, and the beam size is $2\farcs5 \times 2\farcs2$. Both the 610 and 1280 MHz images were corrected for the system temperature (see Omar et al. 2002; Mallick et al. 2012; Vig et al. 2014), and both were rescaled by a correction factor (see Baug et al. 2015; Dewangan et al. 2018).

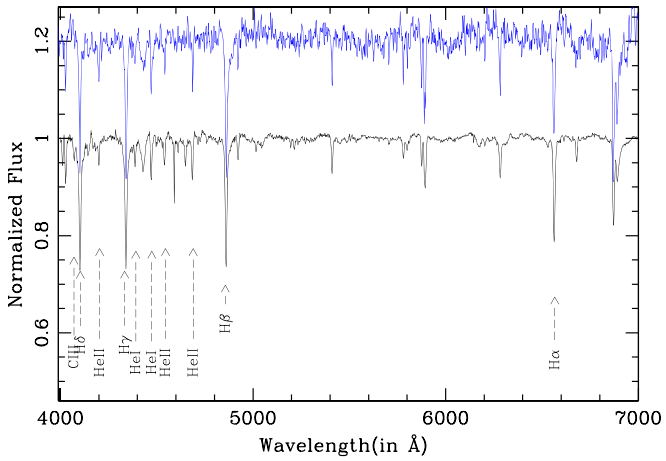

Figure 2. Flux-calibrated normalized spectrum for the optically bright source in Sh2-112. Important spectral lines are marked in the figure. The spectrum of an O8V star (blue curve) from Jacoby et al. (1984) is also shown for comparison.

2.5. Archival Data

2.5.1. Near-IR JHK data from UKIDSS and 2MASS

The UKIRT Infrared Deep Sky Survey (UKIDSS) archival data of the Galactic Plane Survey (GPS release 6.0; Lawrence et al. 2007) are available for the Sh2-112 region. The UKIDSS observations were obtained using the UKIRT Wide Field Camera (WFCAM). Following the selection procedure of the GPS photometry discussed in Dewangan et al. (2015), we retrieved only reliable near-IR (NIR) sources (photometric uncertainty <0.1 mag) in the region. We also used the NIR data from the Two Micron All Sky Survey (2MASS; Cutri et al. 2003). To calibrate the UKIDSS J, H, and K photometric system to the 2MASS system, we rescaled all UKIDSS magnitudes according to their $(J-H)$ and $(H-K)$ UKIDSS colors. We merged the 2MASS and UKIDSS catalogs into a single NIR source catalog, choosing the NIR magnitudes of the fainter sources from the more precise UKIDSS magnitudes. In general, bright sources are saturated in the UKIDSS frames; thus, in the final catalog, the magnitudes for sources brighter than $J \sim 14$ mag are replaced by the 2MASS magnitudes. For further analysis, we considered sources with good photometric magnitudes, i.e., having accuracy better than 10%.

2.5.2. WISE Data

The Wide-field Infrared Survey Explorer (WISE) has mapped the sky in four wave bands (3.4, 4.6, 12, and 22 μm) and uncovered populations of YSO candidates hindered in the dense clouds. We used the WISE catalog from Cutri et al. (2014) to identify YSO candidates in the Sh2-112 region. The spatial resolution at the first three WISE bands is $6''$ and reaches $12''$ at 22 μm. To ensure good-quality photometry, we considered only those sources that have magnitude uncertainties $\leqslant 0.2$ mag and rejected sources with contamination and confusion flags (cc-flags in the catalog) that include "D," "H," "O," or "P." The 3.4 and 12 μm bands include prominent polycyclic aromatic hydrocarbon (PAH) features at 3.3, 11.3, and 12.7 μm (Samal et al. 2007;

Wright et al. 2010) in addition to the continuum emission and hence can be used to get an idea of the photodissociation region (PDR). The 22 μm band can be used to examine the warm dust emission, i.e., the stochastic emission from small grains, as well as the thermal emission from large grains (Wright et al. 2010). The WISE catalog also includes corresponding 2MASS magnitudes in the JHK_s bands of the sources detected in WISE wave bands.

2.5.3. 21 cm Radio Continuum Data from CGPS

We retrieved 21 cm radio continuum data from the Canadian Galactic Plane Survey (CGPS; Taylor et al. 2003) to trace the extension of ionized gas around Sh2-112.

2.5.4. ^{13}CO (J = 3 – 2) Data

The ^{13}CO (J = 3–2) (330.588 GHz; beam $\sim$14″) data were retrieved from the James Clerk Maxwell Telescope (JCMT) archive (ID: M08AU19; PI: Stuart Lumsden). The observations were obtained in the position-switched raster-scan mode of the Heterodyne Array Receiver Program (HARP; Buckle et al. 2009). We utilized the processed integrated ^{13}CO intensity map of the western part of the Sh2-112 region.

2.5.5. Other Data Sets

Optical and NIR images. We utilized the wide-field Hα-, *I*- and *B*-band images from the National Optical Astronomical Observatory (NOAO) archive to trace the extension of the ionized hydrogen and optical morphology of the region.

We also accessed the processed H_2- and *K*-band images from the Canada–France–Hawaii Telescope archive observed with the Caméra Panoramique Proche InfraRouge (CPAPIR; see Artigau et al. 2004) imager attached to the Observatoire du Mont-Mégantic 1.6 m telescope operated by the Université de Montreál, Université Laval. The CPAPIR is based on a 2048 × 2048 pixel^2 Hawaii-2 IR array detector. With a pixel size of 0.″89, it has an FOV of $\sim$30 × 30 arcmin^2.

Gaia DR2 data. We utilized the Gaia Data Release 2 (DR2; Gaia Collaboration et al. 2018) from the European Space Agency (ESA) mission Gaia to estimate the proper motion of the stars and distance of the complex.

3. Results

3.1. Spectral Analysis of the Brightest Source

In order to confirm the spectral type of the brightest source, BD +45 3216, we extracted the low-resolution, one-dimensional spectrum of the source. The flux-calibrated, normalized spectrum of the brightest source in the wavelength range of 4000–7000 Å is shown in Figure 2. For spectral classification of the star, we used the criteria given by Walborn & Fitzpatrick (1990). Spectra of O and B stars have features of hydrogen, helium, and other atomic lines (e.g., O II, C III, Si III, Si IV, Mg II). Hydrogen and helium lines are usually seen in absorption for dwarfs, whereas they may be in emission in supergiants. For the spectral classification of the star, we use hydrogen, He II and He I, lines. The presence of He II lines (4686, 5411 Å) and He II+I (4026 Å) limits the spectral type to O. Moderate nitrogen enhancement indicates a later O-type spectrum. The line ratios of He II 4686 Å/He I 4713 Å; Si IV 4089 Å/He I 4144, 4387, 4471, 4713 Å; and Si IV 4116 Å/He I 4144 Å suggest that the star may be of type O8–O9V. In the case of early-type stars, the ratio of He I 4471 Å/He II 4542 Å is a primary indicator of the spectral type, and the ratio is greater than 1 for spectral types later than O7. The line strength of He II gets weaker for late O-type stars, and He II (4686 Å) is last seen in B0.5-type stars (Walborn & Fitzpatrick 1990). Finally, the spectral type O8V was assigned to the source by a visual comparison to the standard library spectra (Jacoby et al. 1984). For comparison, we also show the spectrum of an O8V star (blue curve) from Jacoby et al. (1984) in Figure 2. Here we note that an uncertainty of ±1 in the subclass identification is expected, as the present analysis is based on the low-resolution spectrum of the star.

3.2. Distance and Reddening toward the Region

We use the proper motions of the sources in the Sh2-112 region from the Gaia DR2 database (Gaia Collaboration et al. 2018) to identify the probable members of the region and further determine the distance to the region. We used bright stars ($G < 19$ mag) within $\sim 27' \times 27'$ with good proper-motion information ($>5\sigma$) to construct the μ_δ-versus-$\mu_\alpha\cos(\delta)$ vector point diagram (VPD). In Figure 3 (top panel), we show the VPD along with the histograms of the proper motions of the stars in the region. The Gaussian distribution fit to the proper motions along the R.A. ($\mu_\alpha \cos(\delta)$) and decl. (μ_δ) resulted in a mean value of −1.62 and −4.78 mas yr^{-1} with a half-width at half-maximum of 1.09 and 2.44 mas yr^{-1}, respectively. Luri et al. (2018) suggested that systematics and correlations in the Gaia astrometric solution tend to overestimate the true distance, and hence a Bayesian approach should be used to properly account for the covariance uncertainties in the parallaxes and proper motions from the Gaia DR2. Bailer-Jones et al. (2018) determined the distances for the stars using a Bayesian inference method. We used the Bailer-Jones et al. (2018) catalog to obtain the distance of the H II region using the distances of all of the stars located within our target area having proper motions within 3σ of the mean values (see Figure 3, bottom panel). The mean distance of the H II region is estimated as $\sim$2.0 ± 0.7 kpc. The proper motions of the massive star ($\mu_\alpha \cos(\delta)$ $\sim$−4.19 ± 0.66 and μ_δ $\sim$−7.227 ± 0.66 mas yr^{-1}) are within 3σ of the mean values.

We have also calculated the spectrophotometric distance to the bright star BD +45 3216. The optical and NIR magnitudes of the source are obtained from the DFOT and 2MASS data, respectively. To estimate the distance to the O8V source, we first obtained the intrinsic color and magnitude of an O8V star ($(B-V)_0 \sim -0.26$ and $M_V = -4.4$ mag) from Martins et al. (2005). We considered the mean R_V of 3.1 for the reddening correction. Accordingly, the $E(B-V)$ of the source was found to be $\sim$0.64 mag. With an absolute magnitude (M_V) of −4.4 and apparent magnitude (V) of 9.06, we estimated the distance to the O8V star to be $\sim$2 kpc. Note that large errors (at least 20%) in these distance estimates could be due to photometric uncertainties and the general extinction law used in the estimation. The spectrophotometric distance is comparable to the estimated distance of the massive star ($\sim 1.8^{+1.7}_{-0.7}$ kpc) derived from the Gaia DR2 data (Bailer-Jones et al. 2018).

In Figure 4, we show the optical color–magnitude diagrams (CMDs) of the sources detected in the region using the DFOT observations. The sources having proper motions within 3σ of the mean proper-motion values are shown with crosses. The blue solid curve represents the zero-age main sequence (ZAMS) from Girardi et al. (2002), corrected for a distance

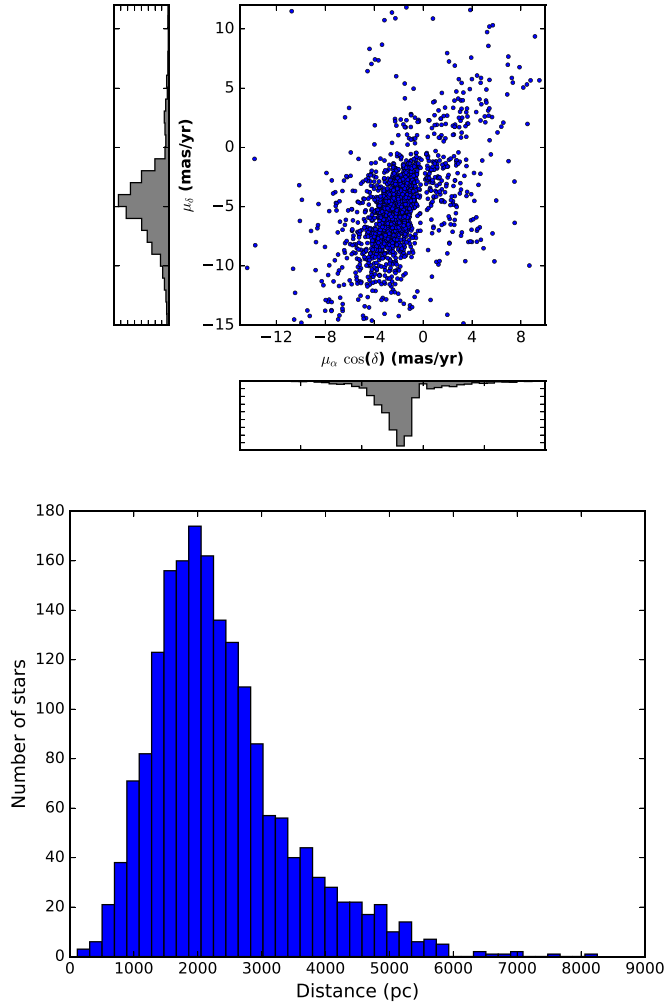

Figure 3. Top panel: histograms of the proper motions of stars in Sh2-112, taken from the Gaia DR2. Bottom panel: histogram of the distances of the stars having proper-motion values within 3σ of the mean proper motions taken from Bailer-Jones et al. (2018).

of ∼2.0 kpc and reddening $E(B-V)$ of ∼0.64 mag, and fits well to the CMDs. We notice a broad distribution of sources in the CMDs that may be due to variable reddening, young stages of stars, binary or field star contamination, etc. However, it is difficult to bifurcate the members of the H II region and field stars based on optical observations only. In the absence of spectroscopic observations, the robust approach to select the sources associated with the region is to identify young stellar content using multiwavelength photometric observations.

3.3. Young Stellar Population in the Region

The young stellar population in an SFR is also helpful to trace the star formation processes in the region. In the present study, we have used the IR data from WISE, 2MASS, and UKIDSS to identify and characterize the young stars in the region. The various schemes are described below.

3.3.1. WISE Color–Color Space

Mid-IR (MIR) wavelengths can penetrate dense material and are useful to unravel the sources in the silhouette of dust layers. In the absence of Spitzer longer-wavelength data, we used the

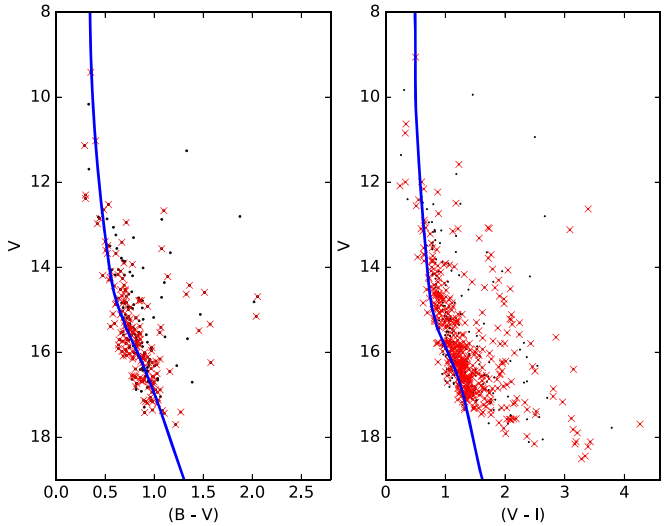

Figure 4. The $(B-V)/V$ (left panel) and $(V-I)/V$ (right panel) CMDs of the sources detected in the region using DFOT observations. The blue solid curves represent the ZAMS from Girardi et al. (2002), corrected for a distance of ∼2 kpc and reddening $E(B-V)$ of ∼0.64 mag. Red crosses represent the sources with proper motions within 3σ of the mean values (see the text).

WISE data for further characterization of the embedded YSO candidates. To remove background contaminants, especially PAH-emitting galaxies and active galactic nuclei (AGN), from the YSO sample, we used the approach developed by Koenig & Leisawitz (2014). This selection method uses a series of color and magnitude cuts to remove contaminants such as star-forming galaxies, AGN, and asymptotic giant branch stars and finally to identify as well as characterize the young stars. To identify the class I and class II candidate sources, we used a sample of the remaining point sources after contamination removal. Based on the WISE colors only, the reddest sources are classified as class I if their colors match all of the following criteria: (i) W2 – W3 > 2.0, (ii) W1 – W2 > −0.42 × (W2 – W3) + 2.2, (iii) W1 – W2 > 0.46 × (W2 – W3) − 0.9, and (iv) W2 – W3 < 4.5.

Sources that were not considered as class I candidates are classified as class II candidates if their colors match all of the following criteria: (i) W1 − W2 > 0.25, (ii) W1 − W2 < 0.9 × (W2 − W3) − 0.25, (iii) W1 − W2 > −1.5 × (W2 − W3) + 2.1, (iv) W1 − W2 > 0.46 × (W2 − W3) − 0.9, and (v) W2 − W3 < 4.5.

We also identified the YSO candidates using the sources having WISE W1 and W2 magnitudes along with the 2MASS H and K magnitudes. These sources are classified as class I candidates if they match all of the following criteria: (i) $H-K>0.0$, (ii) $H-K>-1.76\times(\mathrm{W1}-\mathrm{W2})+0.9$, (iii) $H-K<(0.55/0.16)\times(\mathrm{W1}-\mathrm{W2})-0.85$, (iv) W1 ⩽ 13.0, and (v) $H-K>-1.76\times(\mathrm{W1}-\mathrm{W2})+2.55$.

The sources obeying all of the above conditions except the last one (fifth condition) are classified as class II candidates.

The WISE color–color (CC) diagram for the young stars identified using the WISE and 2MASS color–magnitude criterion in the Sh2-112 region is shown in Figure 5 (top left panel). Open and filled circles represent the class I and class II sources identified based on the WISE/2MASS J, H, and K magnitudes and colors. In total, we identified seven class I and 12 class II sources in the region.

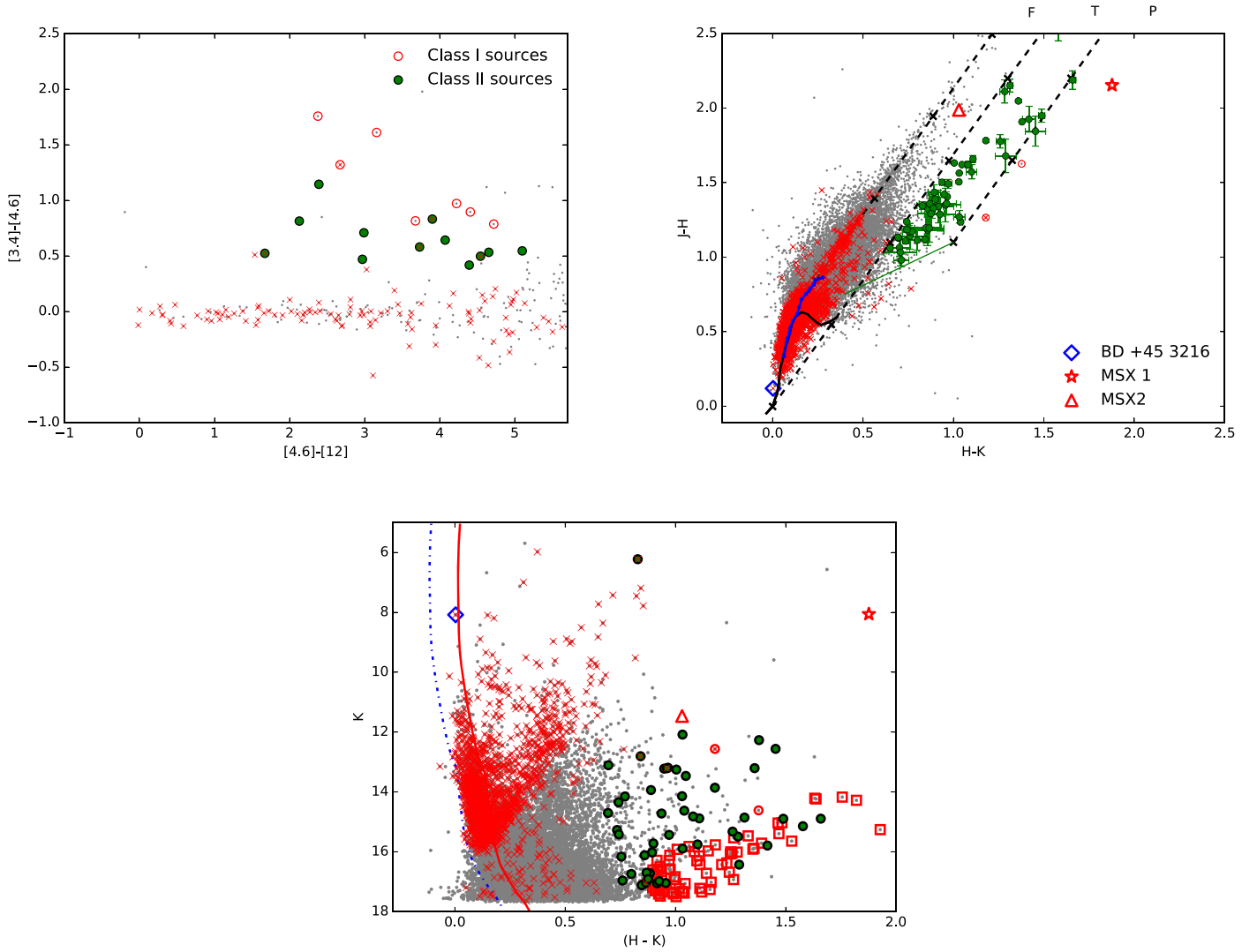

Figure 5. Top left panel: [3.4]–[4.6]/[4.6]–[12] CC diagram for the sources in the Sh2-112 H II region. Filled and open circles represent the class II and class I sources, respectively. Top right panel: $(J-H)/(H-K)$ CC diagram for the sources in the H II region. The thin black curve in the CC diagram represents the MS locus, and the thick blue curve is the locus of the giants (Bessell & Brett 1988). The thin green line is the intrinsic locus of the CTTS (Meyer et al. 1997), and the parallel dashed lines are the reddening vectors drawn from the base of the MS locus, turning point of the MS locus, and tip of the CTTS locus, respectively. Bottom panel: $K/(H-K)$ CMD for the sources in the H II region. In the NIR CC diagram and CMD, filled and open circles are the class II and class I (NIR excess) sources selected based on the NIR CC diagram. Open squares represent the sources with the redder $(H-K)$ color (with higher-magnitude uncertainties in the J band). The dotted–dashed and solid curves are the ZAMS from Girardi et al. (2002) corrected for a distance of ∼2.0 kpc and $A_V = 0$ and 2.0 mag, respectively. The diamond, star, and triangle shown in the NIR CC diagram and CMD represent the massive star BD +45 3216, MSX1, and MSX2, respectively (see Section 3.7). The sources with proper motions within 3σ of the mean values are shown with crosses.

3.3.2. NIR Color–Color Space

The YSO candidates emit excess emission in NIR wavelengths that can be assessed based on their location in NIR color–color space. In Figure 5 (top right panel), we show the NIR $(J-H)/(H-K)$ CC diagram constructed using the combined 2MASS and UKIDSS NIR catalog. The thin black curve in the CC diagram represents the main-sequence (MS) locus, and the thick blue curve is the locus of the giants (Bessell & Brett 1988). The thin green line shows the classical T Tauri star (CTTS) locus (Meyer et al. 1997). The parallel black dashed lines are the reddening vectors drawn from the base of the MS locus, the turning point of the MS locus, and the tip of the CTTS locus, respectively. All of the magnitudes, colors, and loci of the MS, giants, and CTTS are converted to the Caltech Institute of Technology system. We have adopted the extinction laws of Cohen et al. (1981), i.e., $A_J/A_V = 0.265$, $A_H/A_V = 0.155$, and $A_K/A_V = 0.090$. The sources in the NIR CC diagram are classified into three regions, namely, F, T, and P (see Ojha et al. 2004a, 2004b). The sources in the F region are generally considered as MS/evolved field stars or class III YSO candidates (weak-line T Tauri stars), which may be both reddened and unreddened. The sources in the T region are mainly class II YSO candidates (CTTSs; Lada & Adams 1992) with a large NIR excess and/or reddened early-type MS stars with excess emission in the K band (Mallick et al. 2012). The sources in the P region are class I YSO candidates with circumstellar envelopes. However, we note that there may be an overlap of Herbig Ae/Be stars with the sources in the T and P regions, which generally occupy the place below the CTTS locus in the NIR CC diagram (for more details, see Hernández et al. 2005). To decrease contamination to our YSO candidate sample, we do not consider sources that were not falling in the T or P regions within 1σ uncertainty in their colors. Adopting this scheme, we have identified a total of two class I and 54 class II YSO candidates.

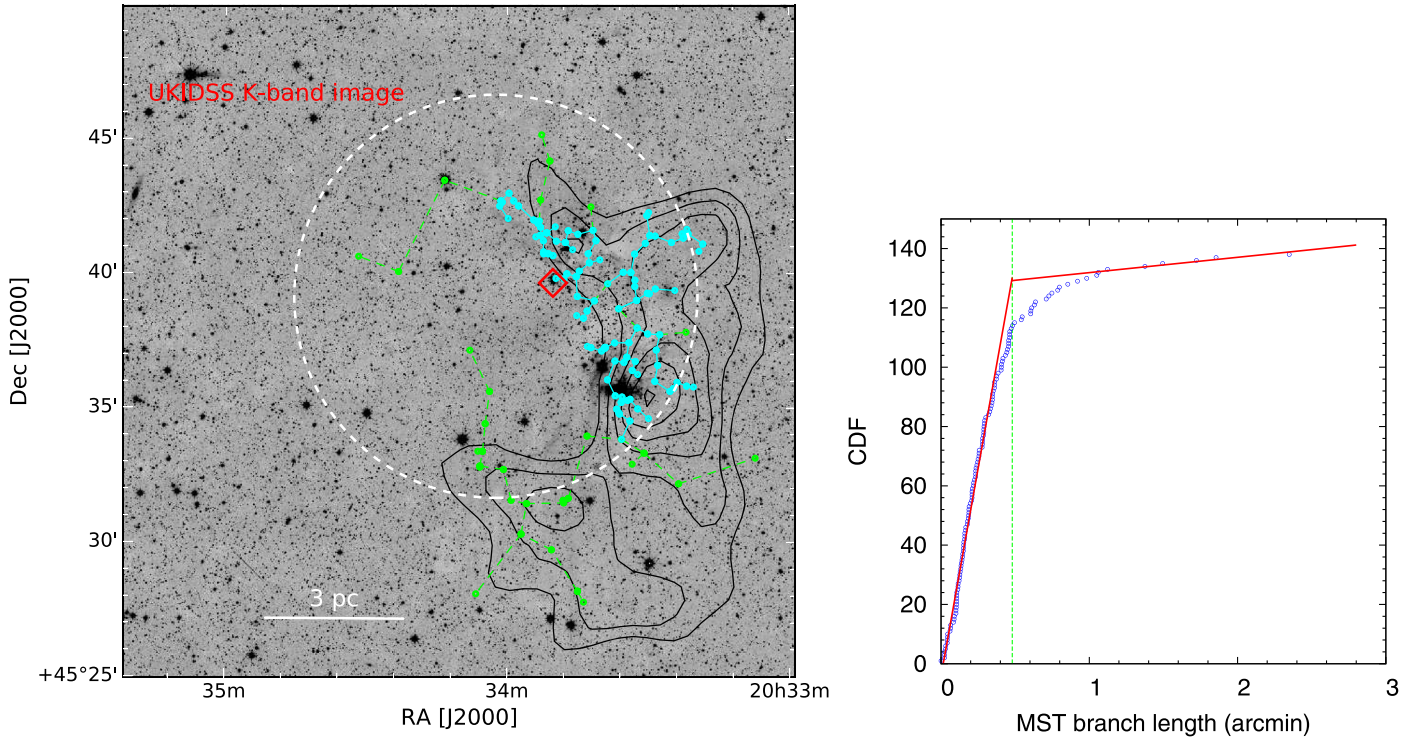

Figure 6. Left panel: UKIDSS *K*-band image of the Sh2-112 region. The MST for the identified YSO candidates in the region is also shown with cyan and green lines. The cyan circles connected with cyan lines and green circles connected with green lines are the branches smaller and bigger than the critical length, respectively. The black contours represent the distribution of the dust extinction in the region. The remaining symbols are similar to those in Figure 1. Right panel: CDF, used for the critical length analysis of YSO candidates. The CDF plot has sorted length values on the *X*-axis and a rising integer counting index on the *Y*-axis. The red solid line is a two-line fit for the CDF distribution. The vertical green line is the critical length obtained for the core region.

3.3.3. NIR Color–Magnitude Space

The NIR CMD is a useful tool to identify a population of YSO candidates with IR excess, which can be easily distinguishable from the MS stars. There may be some YSO candidates that were not detected in the *J* band. Hence, to identify additional YSO candidates in the Sh2-112 region, we also used the *H*- and *K*-band photometry of the sources that do not possess *J*-band photometry or have higher *J*-band magnitude uncertainties (>0.1 mag). Figure 5 (bottom panel) shows the NIR $K/(H-K)$ CMD of the sources in the region. The dotted–dashed and solid curves show the ZAMS loci for a distance of 2.0 kpc with foreground extinctions of $A_V = 0$ and 2 mag, respectively. The NIR excess sources identified based on the NIR CC diagram are shown with open and filled circles. As the UKIDSS catalog is deeper than the 2MASS catalog (Lucas et al. 2008), most of the faint and redder sources seen in the CMD are observed only in the UKIDSS catalog. In the CMD, a low-density gap of sources can be seen at $(H-K)$ ~0.9 mag; therefore, red sources $(H-K > 0.9$ mag) could be the IR excess sources (red sources and presumably YSO candidates). This color criterion is consistent with the control field region, where all of the stars were found to have $(H-K) < 0.9$ mag. A total of 71 sources have been detected as YSO candidates using the $K/(H-K)$ CMD. In Figure 5 (bottom panel), open squares represent the probable IR excess sources identified based on the $K/(H-K)$ CMD. Open and filled circles represent the class I and class II candidates selected based on the NIR CC diagram. The locations of the YSO candidates in the NIR CMD show that a majority of them have a *K* magnitude >11.5 mag, which corresponds to mass $<3\,M_\odot$ (assuming a distance of 2 kpc and an average extinction A_V of ~2 mag and using the 1–2 Myr evolutionary track of Siess et al. 2000).

A few YSO candidates selected using the above methods may have an overlap among them; hence, the YSO candidates detected in the NIR CC diagram and CMD were matched to the WISE YSO candidates. As the resolution of the WISE bands is poor compared to UKIDSS, in a few cases, where there was more than one source within the matching radius, we considered the closest one as the best match. While matching, if the YSO candidate has a different classification in both, priority was given to the classification based on the WISE bands because the longer-wavelength magnitude provides more robust information about the class of the YSO. Eight YSO candidates were found in common in the WISE and NIR catalogs of YSO candidates. In total, we identified 138 class I/II sources in the whole region. The spatial distribution of the YSO candidates is shown with filled circles in Figure 6. We found six Hα emission stars within the HCT FOV, and one of them is a class II source. A sample list of the YSO candidates with their magnitudes in the NIR and WISE bands is given in Table 2, and the entire table is available in electronic form only.

3.4. Clustering of YSO Candidates

To study the density distribution of YSO candidates in the Sh2-112 region, we have generated the surface density map using the nearest-neighbor (NN) method (e.g., Gutermuth et al. 2009) with a grid size of 15″ and the six nearest YSO candidates. The YSO surface density map obtained by this method is shown as black contours overlaid on the WISE W3 and W4 and Hα color-composite image of the H II region in Figure 7(b).

The surface density contours clearly reveal the subclustered and filamentary distribution of YSO candidates near the western periphery, presumably due to the fragmentation of the filamentary molecular cloud. The physical parameters of these subclusters,

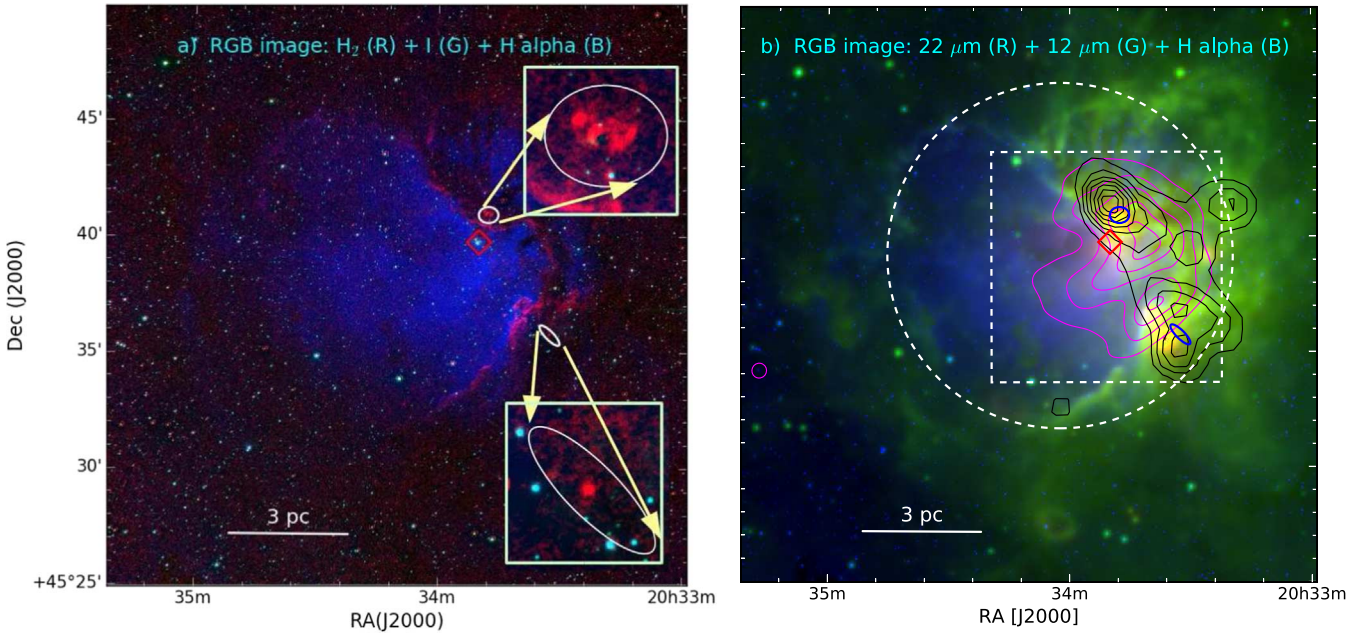

Figure 7. (a) Color-composite image of the Sh2-112 region generated from the H_2 (red), *I*-band (green), and Hα (blue) images. Ellipses show the locations of the H_2 knots. (b) Color-composite (WISE 22 μm: red; 12 μm: green; KPNO Hα: blue) image of the Sh2-112 region. The magenta contours show the distribution of the GMRT 610 MHz radio continuum emission from a level of 50 mJy beam^{-1} to the peak value of 330 mJy beam^{-1} with an increment of 50 mJy beam^{-1}. The black contours represent the surface density distribution of the YSO candidates in the region. Other symbols are similar to those in Figure 1.

Table 2
YSO Candidates from 2MASS/UKIDSS and WISE Data

ID	R.A. (J2000)	Decl. (J2000)	$J \pm eJ$	$H \pm eH$	$K \pm eK$	[3.4] ± e[3.4]	[4.6] ± e[4.6]	[12] ± e[12]	[22 ± e[22]	Flag
1	308.43758	45.469861	18.43 ± 99.99	17.24 ± 99.99	15.12 ± 0.13	11.90 ± 0.02	10.14 ± 0.02	7.76 ± 0.02	4.79 ± 0.03	WISE
2	308.35136	45.656319	15.01 ± 0.04	13.56 ± 0.03	12.91 ± 0.03	11.96 ± 0.07	11.14 ± 0.04	7.47 ± 0.06	2.45 ± 0.03	WISE
3	308.416255	45.618854	17.58 ± 99.99	15.508 ± 0.13	13.72 ± 0.05	10.53 ± 0.02	9.75 ± 0.02	5.03 ± 0.01	2.04 ± 0.03	WISE

(This table is available in its entirety in machine-readable form.)

which might have formed in a single star-forming event, play a very important role in the study of star formation. We further used minimal spanning tree (MST)–based techniques to isolate these subclusters of YSO candidates from their scattered distribution. The MST is defined as the network of lines or branches that connect a set of points together such that the total length of the branches is minimized and there are no closed loops. This technique efficiently isolates the substructures without any type of smoothening and bias regarding the shapes of the distribution (Gutermuth et al. 2009). This method also preserves the underlying geometry of the distribution (e.g., Cartwright & Whitworth 2004; Schmeja & Klessen 2006; Gutermuth et al. 2009; Sharma et al. 2016).

To obtain the MSTs for the YSO candidates in the region, we used the approach suggested by Gutermuth et al. (2009) and Sharma et al. (2016). In Figure 6 (left panel), we have overplotted the derived MSTs for the location of YSO candidates in Sh2-112. The circles and lines denote the positions of the YSO candidates and MST branches, respectively. The MST distribution also clearly shows the subclusters near the western periphery of the H II region. To isolate these subclusters of YSO candidates, we determined the critical branch length of the MST by plotting their cumulative distribution. The resultant cumulative distribution function (CDF) in Figure 6 (right panel) clearly shows a three-segment curve: a steep-sloped segment at short spacings, a transition segment that approximates the curved character of the intermediate-length spacings, and a shallow part. We have fitted two lines in the shallow and steep segments and extend these two to connect together. We adopted the intersection point between these two lines as the MST critical branch length (see also Gutermuth et al. 2009; Chavarría et al. 2014; Sharma et al. 2016). The YSO subclusters were then isolated from the lower-density distribution by clipping MST branches longer than the critical length found above. The value of the critical branch length for the subclusters is 0.′48, which is shown as a vertical line. Cyan circles and MST connections in Figure 6 (left panel) represent the locations of YSO candidates in the subclusters identified using the above procedure.

3.5. Optical Morphology of the Region

The Hα emission from the region traces the possible extension of the H II region, which can be seen in blue in Figure 7(a). Though the H II region in general represents the spherical morphology, we notice that the massive star is not at the center of the H II region, and Hα emission is extended only toward the eastern side of the massive star. There are dark features visible against the bright Hα emission of the H II region. An elongated obscuring dark lane extending approximately in the northwest-to-southwest direction near the western periphery is seen. This obscuring dark lane suggests the probable presence of the molecular cloud. The southwest part is brighter and has a sharp

arc-like structure in the western direction, giving an impression of a possible ionization front (IF), whereas the northern part has an extended and very filamentary structure with a stunning view of the dust content, indicating that a significant amount of dust is concentrated in the filaments across the region. This structured feature suggests an inhomogeneous spatial distribution of the interstellar matter. In addition, we notice patchy, faint Hα nebulosity to the west of the H II region.

3.6. Distribution of Shocked H_2 Emission

The high-excitation molecular gas can be probed using the NIR H_2 line emission at 2.12 μm. A continuum-subtracted H_2 line emission image was obtained by removing the offline emission using the *K*-band image. For this, first, the image with the best seeing was degraded by convolution with a Gaussian function using the IRAF task *psfmatch* to match the width of the PSF in different images. For the *K*-band image, a flux scaling factor was derived by comparing the counts of several stars in both images, and then an H_2 emission image was obtained by subtracting the *K*-band scaled image from the H_2 image.

In Figure 7(a), the distribution of continuum-subtracted H_2 emission in Sh2-112 is shown in red. In the continuum-subtracted H_2 image, compact features with a combination of positive and negative valued features are the residuals of continuum subtraction of point sources. In addition to those features, values lower than the background are observed. This is due to the continuum, whose flux ratio between the H_2 narrowband and *K*-band filters is different from that of foreground stars. Figure 7(a) reveals diffuse H_2 emission along the western border of the H II region, as well as notable features at various locations of the nebula. The diffuse H_2 emission can arise due to either the UV fluorescence from the massive star (and thus can trace the PDR) or collisional excitation by the shocks from outflows originating from nearby YSO candidates (e.g., Chrysostomou et al. 1992). The PDR can also be traced by the PAH emission in the WISE 12 μm band. However, the close resemblance of the H_2 emission to the 12 μm emission (see Figure 7) suggests that H_2 emission features at the western periphery of Sh2-112 are more likely caused by excitation from UV photons. Also, the H_2 emission shows rim- or arc-like morphology, with either the rim facing toward the ionizing source or the curvature of arc appearing to be created by the UV photons from the ionizing star. However, high-resolution and high-sensitivity molecular line observations are needed to shed more light on this. The morphology of H_2 is different compared to the ionized gas emission traced by the Hα image. The H_2 is seen at the edges of the ionized gas emission, while there is little or no emission in the central region (see Figure 7(a)). This indicates the presence of highly excited molecular gas around the western periphery of the H II region. In addition to the filamentary structures, a few H_2 knots are also visible in this region (see the features surrounded by ellipses in Figure 7).

The massive star located in this region and its high-energy feedback might be responsible for H_2 and PAH emissions and the observed arc-like morphology of gas and dust.

3.7. Distribution of the Ionized Gas

As the ionized gas of the H II region emits in the radio continuum due to free–free (bremsstrahlung) radiation, the radio continuum images can be used to trace the distribution of the ionized gas in the H II region. In Figure 1, the distribution of 21 cm radio continuum emission from CGPS is shown in blue. The distribution of continuum emission suggests a complex morphology of the ionized gas emission. The location of a previously characterized O8V star (BD +45 3216) does not appear near the peak of the radio continuum emission. The bulk of the ionized emission is located toward the western periphery. To better understand this region, we have further used the GMRT data at 610 and 1280 MHz, which have better resolution and sensitivity than the CGPS 1420 MHz data.

The GMRT radio contours at 610 MHz (magenta contours) are overlaid on a color-composite image (WISE 22 μm: red; 12 μm: green; Hα: blue) of the Sh2-112 H II region in Figure 7(b). Furthermore, the correlation of the warm dust and ionized emission is also evident, which has generally been found in the H II regions (e.g., Deharveng et al. 2010; Paladini et al. 2012). In addition to the extended emission, the embedded stellar contents are seen near and around the arc-like structure.

Figure 8 shows the zoomed-in view of the square region (∼10′ × 10′) shown in Figure 7(b). In Figure 8 (top left panel), we overlaid the GMRT 1280 MHz contours on the inverted H_2 image. It is clear from Figure 7(b) that the ionized emission associated with this H II region displays a complex morphology at 610 MHz with a steep intensity gradient toward the west. A faint, broad, and diffuse emission is seen toward the northwest. The 610 MHz emission contours at the western periphery seem to be made up of three components in the 1280 MHz emission: a clearly visible arc-shaped structure toward the southwest boundary, an extended filamentary feature above the arc-shaped structure, and a compact source toward the north of the massive star BD +45 3216. This compact radio source at 1280 MHz could possibly be a compact/ultracompact (UC) H II region.

In this UC H II region, the free–free emission at 1280 MHz is assumed to be optically thin, and considering that the region is in photoionization equilibrium, the total number of ionizing photons ($N_{\rm UV}$) from the massive source is obtained by using the integrated radio flux within the region (S_ν), following the equation given in Morgan et al. (2004), i.e.,

$$N_{\rm UV} = 7.7 \times 10^{43} S_\nu D^2 \nu^{0.1}, \quad (1)$$

where S_ν is in mJy, D is the distance to the source in kiloparsecs, and ν is the frequency of the observation in GHz. The estimated Lyman continuum flux for the UC H II region is $10^{47.1}$ photons s^{-1} for a distance of ∼2 kpc, which corresponds to a single ionizing star of spectral type B0–B0.5 V (see Table 2 of Panagia 1973). As the optical images do not show any source corresponding to the radio continuum peak, however, longer-wavelength images reveal the presence of a source inside it, suggesting that the massive star is still embedded within the molecular material.

An extended filamentary feature above the arc-shaped structure (see Figure 8, top left panel) also appears as the enhanced Hα emission, as seen in Figure 8 (bottom right panel). However, this feature is not visible in the WISE 12 μm image and seems to be due to the high intensity of ionized gas emission.

The location of a noticeable arc-like feature in the radio emission contours matches very well with the curved bright emission feature in the Hα image. This positional and morphological correlation of arc-like structure in radio and optical images suggests that the radio emission may be originating from the ionized boundary layer (IBL) located at the border of the dark molecular cloud. The IBL is a recombination layer that develops on the side of the cloud facing the ionizing star when the surface of the molecular cloud becomes ionized. Thus, the radio emission map at 1280 MHz is utilized to

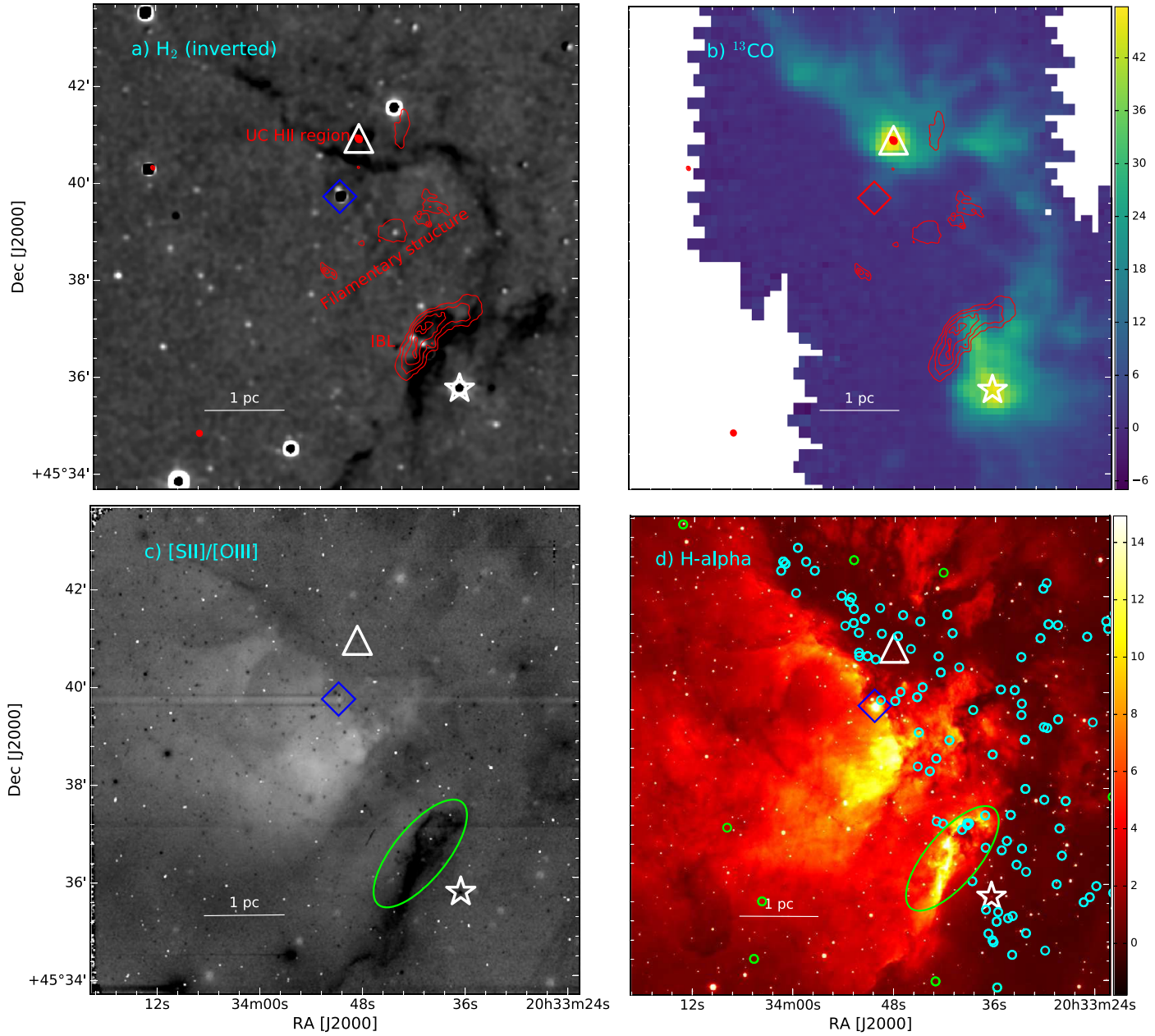

Figure 8. Zoomed-in view of the square region ($\sim 10' \times 10'$) shown in Figure 7(b). Panel (a): H_2 inverted gray-scale map. Panel (b): ^{13}CO intensity map. Panel (c): [S II]/[O III] ratio gray-scale map. Panel (d): Hα intensity map of the Sh2-112 region. The distribution of 1280 MHz emission obtained from the GMRT observations is shown as red contours at a level starting from 0.3 mJy beam^{-1} to the peak value of 23 mJy beam^{-1} with an increment of 0.125 mJy beam^{-1}. The circles in panel (d) represent the spatial distribution of the young stars. Stars and triangles represent MSX sources MSX1 and MSX2, respectively. The ellipse in the bottom panels shows the location of the IBL. The remaining symbols are similar to those in Figure 1.

estimate the ionizing flux (ϕ_p) impinging on the curved rim-like feature and the electron density (n_e) within the IBL.

We calculated the ionizing flux and electron density using the equations given in Lefloch et al. (1997) and Thompson et al. (2004):

$$\phi_p = 1.24 \times 10^{10} S_\nu T_e^{0.35} \nu^{0.1} \theta^{-2}, \quad (2)$$

$$n_e = 122.41 \times \sqrt{\frac{S_\nu T_e^{0.35} \nu^{0.1} \theta^{-2}}{\eta R}}, \quad (3)$$

where T_e is the effective electron temperature of the ionized gas in K, ν is the frequency of the free–free emission in GHz, θ is the angular diameter over which the emission is integrated in arcseconds, and R and η are the radius of the cloud in parsecs and the effective thickness of the IBL as a fraction of the cloud radius, respectively. Here η was found to vary in the range 0.1–0.2 of the cloud radius and is primarily dependent upon the ionizing flux and cloud curvature (Bertoldi 1989). Here we have taken $\eta = 0.2$, which implies that the derived electron density of R is taken as $\sim$0.8 pc. We derived the photon flux value (ϕ_p) of 2.34×10^{10} cm^{-2} s^{-1}, which is larger than the ionizing flux predicted (1.25×10^{10} cm^{-2} s^{-1}) at this location due to an O8 V star. This excess of the measured ionizing flux may be due to another embedded radio source. The WISE 22 μm image reveals

extended emission from a point source near the IBL, further strengthening the possibility of an embedded radio source near the IBL. We obtained an electron density of ∼413 cm^{-3}, which is greater than the critical value of ∼25 cm^{-3} above which an IBL is able to develop around a molecular cloud (see Lefloch & Lazareff 1995).

We looked for the Midcourse Space Experiment (MSX) point sources toward the UC H II region and IBL. We found a source, MSX 6C 083.7071+03.2817 (hereafter MSX1), ∼1′ away from the IBL and another source, MSX 6C 083.7962+03.3058 (hereafter MSX2), near the UC H II region. The locations of MSX1 and MSX2 are shown in Figure 8 as stars and triangles, respectively. We also looked for the 2MASS counterparts of MSX1 and MSX2. The locations of these two sources are shown in the NIR CC diagram and CMD (see Figure 5). We note that the magnitude uncertainty associated with the 2MASS magnitudes of MSX2 is higher. The $H/(H-K)$ CMD shows that these sources (MSX1 and MSX2) could have foreground extinction, A_V, of ∼21 and 19 mag, respectively. The NIR CMD shows that MSX2 may be of B1–B2 spectral type, which is comparable to that obtained based on the radio continuum emission at 1280 MHz.

Urquhart et al. (2009) also observed a compact VLA source at 6 cm radio continuum emission toward MSX2 and designated it a compact H II region. Cooper et al. (2013) carried out NIR spectroscopy of massive YSO candidates in several SFRs, including MSX1. They classified MSX1 as a massive YSO candidate with a luminosity of ∼5.7×10^3 $L_\odot$ embedded in extinction of $A_V \sim$ 26–36 mag. Further in the direction of the western periphery of the Sh2-112 H II region (∼4′ away from MSX1), another compact radio continuum source can be seen that was also observed by Urquhart et al. (2009) at the 6 cm VLA observations.

The dynamical age of the H II region can be estimated using the equation given in Dyson & Williams (1980),

$$t_{\rm dyn} = \left(\frac{4\,R_s}{7\,c_s}\right)\left[\left(\frac{R_{\rm HII}}{R_s}\right)^{7/4} - 1\right], \quad (4)$$

where c_s is the isothermal sound velocity in the ionized gas ($c_s = 10$ km s^{-1}; Bisbas et al. 2009), $R_{\rm H\,II}$ is the radius of the H II region, and R_s is the radius of the Strömgren sphere calculated using the equation

$$R_s = (3N_{\rm UV}/4\pi n^2 \alpha_B)^{1/3}, \quad (5)$$

where the radiative recombination coefficient $\alpha_B = 2.6 \times 10^{-13}$ $(10^4\ {\rm K}/T)^{0.7}$ cm^3 s^{-1} (Kwan 1997), $N_{\rm UV}$ is the number of UV photons s^{-1}, and n is the initial particle number density of the ambient neutral gas. Considering a typical value of $N_{\rm UV}$ for an O8V star from Panagia (1973) and $R_{\rm H\ II}$ as 7.′5, the calculated dynamical age might vary substantially, depending on the initial density. The dynamical age of the H II region Sh2-112 varies from 1.6 to ∼5 Myr for a range of ambient density (n) of 10^3–10^4 cm^{-3}. We also calculated the dynamical age of the UC H II region. Assuming n (=10^5 cm^{-3}), we estimated the dynamical age of the UC H II region as 0.01 Myr.

3.8. Distribution of Molecular Gas and Cold Dust

The molecular hydrogen gas in the SFRs can be detected via CO observations. Dobashi et al. (1994) undertook CO observations of the whole Cygnus complex, including H II region Sh2-112. Their low-resolution CO maps show the presence of the CO emission in the direction of Sh2-112. In the absence of high-resolution CO observations, dust content via extinction measurement is a direct and reliable tracer of the hydrogen content of the molecular clouds. The extinction measurements can be done by measuring the color excess in the IR wavelengths (Lada et al. 1994). To generate the dust extinction map for the Sh2-112 region, we used our NIR catalog and followed the method discussed in Panwar et al. (2014). The region was divided into a number of small cells, and we looked for the $(H-K)$ colors of the 20 nearest stars to the cell center. We computed the color excess $E = (H-K)_{\rm obs} - (H-K)_{\rm int}$, where $(H-K)_{\rm obs}$ is the observed median color in a cell and $(H-K)_{\rm int}$ is the intrinsic median color estimated from the colors of supposedly unreddened stars. We calculated the extinction in the K band (A_K) within each cell using the relation $A_K = 1.82E$ (Flaherty et al. 2007). Further, the A_V value is obtained using the relation $A_V = 15.87E$. The extinction map for the H II region is plotted in Figure 6 (left panel) as black contours. The contours start with 25% of the peak value with an increment of 15%. The average spatial resolution of the extinction map is ∼30″ (which converts to 0.3 pc at 2 kpc distance). However, the resolution of the extinction map depends on the surface density of the stars and is higher for the regions with high surface density and lower for the regions with low surface density. The main factors contributing to the uncertainty in the extinction measurement are the random error in the measurement of $(H-K)$ colors and the systematic error due to the adopted extinction law. The extinction map clearly indicates that the dust is present toward the western periphery of the H II region. The deficit of the dust content and subsequently molecular material toward the eastern part may be due to escaping ionized hydrogen gas in this direction.

The distribution of molecular gas in SFRs is clumpy in general. As the ^{13}CO line is more optically thin compared to the ^{12}CO line, the ^{13}CO line data can trace dense condensation and its associated velocity better than ^{12}CO. A JCMT ^{13}CO image of the western periphery of the H II region (near the source MSX1 and MSX2) integrated in the [−16, −1] km s^{-1} velocity range is shown in Figure 8 (top right panel). This region also appears to be associated with H_2 and/or PAH features (see Figure 7), suggesting a close interaction between ionized and molecular gas in the complex. As NH_3 is generally used as a high-density gas tracer, Urquhart et al. (2011) observed the MSX sources MSX1 and MSX2 for NH_3 (1,1), (2,2), and (3,3) and water maser emissions and detected NH_3 emission toward both MSX sources, whereas the water maser was observed only toward MSX1. Maud et al. (2015b) also detected massive molecular outflows toward MSX1 and found that the dynamical timescale of the redshifted and blueshifted lobes of the outflows is of the order of 4×10^4 yr. They also suggested that MSX2 is also probably associated with the molecular outflows. The ^{13}CO observations by Urquhart et al. (2009) revealed a component of $V_{\rm LSR} \sim -3.2$ km s^{-1} associated with MSX1, whereas two components of $V_{\rm LSR}$ −11.6 and −3.7 km s^{-1} are associated with MSX2. Maud et al. (2015a) also observed strong $C^{18}O$ emission toward these sources. Thus, the western side of the H II region seems to possess molecular gas and dense cores and be associated with recent/ongoing star formation activity.

4. Discussion

4.1. Sh2-112: A Candidate Blister H II Region

An H II region develops a spherical morphology if the massive star forms in a uniform molecular cloud. However, if the massive

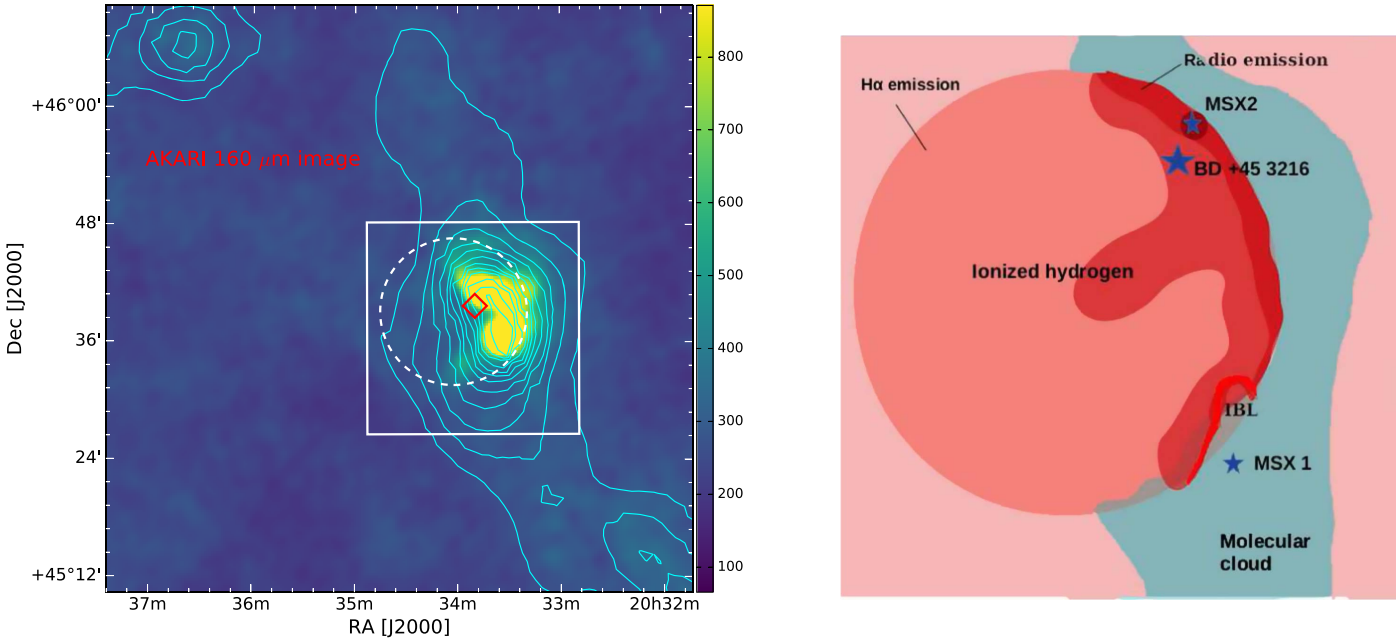

Figure 9. Left: AKARI 160 μm image superimposed by Planck 353 GHz contours. The contours start from 0.033 mJy sr^{-1} with a step size of 0.005 mJy sr^{-1}. Right: cartoon diagram representing the morphology of the H II region Sh2-112 within the white box shown in the left panel.

star forms close to the edge of a molecular cloud, the expanding IF/SF quickly reaches the edge of the cloud. Consequently, the H II region opens in the direction away from the cloud edge (Tenorio-Tagle 1979; Henney et al. 2005; Krumholz & Matzner 2009), as ionized gas would be less confined and could easily stream out into the lower-density interstellar medium (ISM). It rapidly propagates through the low-density ISM, followed by a strong shock driven by the higher-pressure ionized cloud material. At the same time, a rarefaction wave propagates back into the ionized cloud, giving rise to a "blister-type" H II region showing the champagne flow of ionized material (see, e.g., Duronea et al. 2012; Maheswar et al. 2007). The Sh2-112 H II region represents a spherical shell of a diameter of $\sim$15′ ($\sim$8.7 pc, at the distance of $\sim$2 kpc). The ^{13}CO and extinction maps suggest the presence of molecular gas near the western periphery of the H II region. This molecular material also appears as a highly extinct dark lane in the optical Hα image (see Sections 3.7 and 3.8), where most of the YSO candidates identified in the present work are located. As described in Sections 3.6 and 3.7, the H_2 and PAH emission, indicating the location of the PDR, encircles the western border of the H II region. A curved morphology of the radio continuum emission in the western periphery further suggests a stalling effect for the ionized gas against the PDR in that direction.

As shown by Pellegrini et al. (2012), the [S II]/[O III] ratio map can be used to distinguish density-bounded, radiation-bounded, and blister-type H II regions. Pellegrini et al. (2012) found that the optically thick nebula with highly ionized gas (low [S II]/[O III] ratio; appears dark in ratio map) is usually surrounded by an ionization transition zone with a higher [S II]/[O III] ratio (appears as lighter gray scale). We made an [S II]/[O III] ratio map of the central part ($\sim$10′ × 10′) of the Sh2-112 H II region, which is shown in Figure 8 (bottom left panel). The ratio map consists of bright and dark features. We notice a pronounced ionization transition zone (bright region) toward the south of the massive star, where Hα emission is traced. This ionization transition zone appears to be surrounded by a relatively diffuse feature in light gray. In the southwestern direction, the ratio of [S II]/[O III] reveals the presence of ionized gas (dark feature) in the region, which is spatially correlated with the IBL. The distribution of the ionized hydrogen, H_2, and ^{13}CO emission indicates that the IBL structure is seen edge-on. An example of this kind of edge-on geometry is the Orion bar, which is located in a blister-type H II region, the Orion Nebula (Goicoechea et al. 2018). In our case, the bright S II emission could actually be on the surface of the H II cavity. Therefore, from the above analysis, it seems that Sh2-112 is an example of a blistered H II region that is ionization-bounded on the high-density sides (western direction) and density-bounded on the low-density sides (eastern direction). The intensity gradient of the radio emission (see 610 MHz emission contours in Figure 7(b)) supports that the ionized gas is escaping from the H II region toward the low-density ISM in the eastern direction. Based on radial velocity measurements of the Hα (i.e., $-$9.7 km s^{-1}) and CO (i.e., $-$12.2 km s^{-1}) emissions, Israel (1978) also suggested that the ionized gas in the Sh2-112 region is probably undergoing a champagne flow.

Thus, the structure of the radio continuum, dust extinction, ^{13}CO, and [S II]/[O III] ratio maps; the spatial distribution of the young stars; and the NIR-to-MIR images of the H II region indicate that Sh2-112 is a blistered H II region in which the ionized gas is possibly undergoing a champagne flow.

In Figure 9, we show the AKARI 160 μm image superimposed by Planck 353 GHz contours (left panel) and a simple geometry of the H II region (right panel). Based on the distribution of the cold dust emission and young stars, we suggest that the massive star possibly formed on the eastern edge of a cylindrical molecular cloud. It has ionized the surrounding molecular material and created the H II region. As the IF from the massive star reached the cloud surface, it broke the cloud boundary and quickly expanded to the eastern side (low-density ISM), while, on the western side of the ionizing star, the expansion is slow, probably due to a higher-density molecular cloud. In the northwest boundary, a UC H II region is created by a massive member that is still embedded in the molecular cloud. Some of the YSO candidates observed toward

the western periphery may have originated due to the interaction of the expanding H II region with the surrounding molecular cloud. However, with the present observations, it is difficult to disentangle the YSO candidates formed via a triggered or spontaneous star formation scenario.

4.2. Star Formation toward the Southwest: Possible Case of Triggering?

To study the influence of the massive O8V star on MSX1, we estimated the ionized gas pressure in the IBL and the internal pressure of the molecular condensation. A comparison of these pressures can be used as a sensitive diagnostic for the induced star formation within the molecular cloud (Lefloch & Lazareff 1994; Morgan et al. 2004). If the internal pressure of the cloud is higher with respect to the IBL, then the photoionization-induced shock will be stalled at the surface; hence, it is highly unlikely that any star formation activity observed within the cloud is due to triggering from the massive star. Conversely, if the cloud is underpressured with respect to the IBL, then there is a high possibility that photoionization-driven shocks are propagating or have already propagated through the molecular cloud, and consequently, the star formation within the clouds could have been induced due to the radiative feedback effect of a massive star. Following Thompson et al. (2004), the ionized gas pressure for the IBL is estimated using the equation

$$P_i/K_B = 2n_eT, \tag{6}$$

where n_e is the electron density (see Equation (3)), and K_B is the Boltzman constant. We obtained a value of $\sim 8 \times 10^6$ cm^{-3} K for P_i/K_B. To estimate the internal pressure of the molecular condensation, we adopted the following relation:

$$P_{\rm int}/K_B \sim \sigma^2\rho_{\rm int}, \tag{7}$$

where $\rho_{\rm int}$ is the internal density of the molecular condensation and σ is the velocity dispersion. The value of σ^2 is estimated using the relation $\sigma^2 = \Delta v^2/(8\ln 2)$, where Δv is the line width of the ^{13}CO ($J = 3 - 2$) line taken from Urquhart et al. (2009). Here we assumed a number density of the molecular condensation, $n(H_2)$, of 10^3 cm^{-3}. This yields a value of $P_{\rm int}/K_B$ as $\sim 7.3 \times 10^5$ cm^{-3} K. The main factors contributing to the uncertainties in the ionized gas pressure value are the electron density and the temperature of the ionized gas. The uncertainties involved in the calculation of electron density depend on the assumption of η and the distance. The combined error of both of them may be about 40% (Ortega et al. 2013). Similarly, the uncertainties involved with the value of internal molecular pressure include the uncertainties in the line width measurements and radius of the cloud. In the case of a sample of bright-rimmed clouds, Morgan et al. (2004) estimated uncertainties in the internal molecular pressures that were no more than a factor of 5.

A comparison between internal and ionized gas pressures indicates that the IBL is overpressured with respect to the molecular condensation by a factor of 10, suggesting that shocks are propagating/propagated through the molecular condensation, and the young stars identified within it are likely triggered due to the massive star BD +45 3216. Since the ionizing source is an O8V star, still on the MS, it should have an MS lifetime of <5 Myr (Meynet et al. 1994). This suggests that the H II region may still be under expansion and may be responsible for triggering next-generation star formation.

5. Conclusions

The complex nature of the H II region Sh2-112 has made it a very intriguing and poorly studied H II region. Understanding the ongoing physical processes in such a complex region requires a thorough multiwavelength analysis. In the present work, we study the physical environment of the Galactic H II region Sh2-112 using multiwavelength observations. We use optical and NIR photometric and spectroscopic observations, as well as radio continuum observations. Our main findings are as follows.

1. The analysis of the optical spectra of the bright source BD +45 3216 confirms that it is of O8 V type.
2. Using various NIR/MIR CC diagrams and CMDs, we identified a total of 138 YSO candidates in the region. Out of these, eight are class I objects, 59 are class II objects, and the remaining 71 are sources with IR excess ($H - K > 0.9$) which could be candidate class II/class I YSO candidates. The $H/(H - K)$ CMD analysis shows that the majority of YSO candidates have masses less than 3 $M_\odot$.
3. The NN surface density distribution and MST analyses of YSO candidates reveal the grouping of YSO candidates toward the western periphery.
4. The high-resolution 1280 MHz radio continuum map reveals a peak near the northwest periphery of the Sh2-112 region, which may be a UC H II region excited by a B0V–B0.5V star. Optical (Hα) and radio images show the presence of an IBL and molecular cloud emission at ^{13}CO toward the southwest periphery. This region also consists of a group of young stars.
5. We estimated the pressures in the IBL and molecular clump and found that the IBL is overpressured with respect to the molecular condensation, suggesting that the photoionization-driven shocks are propagating/propagated inside the molecular condensation and the star formation observed inside it may be due to the triggering by the massive star. The distribution of the dust emission, radio continuum emission, [S II]/[O III] ratio map, and surface density distribution of the YSO candidates suggest that Sh2-112 is a blister H II region that may have formed in a cylindrical molecular cloud.

We thank the anonymous reviewer for a critical reading of the manuscript and constructive suggestions that greatly improved its quality. N.P. acknowledges financial support from the Department of Science & Technology (DST), India, through INSPIRE faculty award IFA-PH-36. S.S. and N.P. acknowledge the support of the DST, Government of India, under project No. DST/INT/Thai/P-15/2019. D.K.O. acknowledges the support of the Department of Atomic Energy, Government of India, under project identification No. RTI 4002. T.B. is supported by the National Key Research and Development Program of China (2017YFA0402702). T.B. also acknowledges funding from the China Postdoctoral Science Foundation through grant 2018M631241 and the PKU-Tokyo Partner fund. The research work at Physical Research Laboratory is funded by the Department of Space, Government of India. We thank the staff of IAO, Hanle, and CREST, Hosakote, that made these observations possible. The facilities at IAO and CREST are operated by the Indian Institute of Astrophysics, Bangalore. We are thankful to the JTAC and staff of the 1.3-m DFOT operated by ARIES. This publication makes use of data from the Two Micron All Sky Survey (a joint

project of the University of Massachusetts and the Infrared Processing and Analysis Center/California Institute of Technology, funded by the National Aeronautics and Space Administration and the National Science Foundation) and archival data obtained with the Wide-field Infrared Survey Explorer (operated by the Jet Propulsion Laboratory, California Institute of Technology, under contract with NASA). This work is based on data obtained as part of the UKIRT Infrared Deep Sky Survey. This research uses services or data provided by the Science Data Archive at NOAO. NOAO is operated by the Association of Universities for Research in Astronomy (AURA), Inc. under a cooperative agreement with the NSF.

ORCID iDs

Neelam Panwar https://orcid.org/0000-0002-0151-2361
Saurabh Sharma https://orcid.org/0000-0001-5731-3057
D. K. Ojha https://orcid.org/0000-0001-9312-3816
T. Baug https://orcid.org/0000-0003-0295-6586
L. K. Dewangan https://orcid.org/0000-0001-6725-0483
Rakesh Pandey https://orcid.org/0000-0002-7485-8283

References

Artigau, E., Doyon, R., Vallee, P., Riopel, M., & Nadeau, D. 2004, Proc. SPIE, 5492, 1479
Bailer-Jones, C. A. L., Rybizki, J., Fouesneau, M., Mantelet, G., & Andrae, R. 2018, AJ, 156, 58
Baug, T., Ojha, D. K., Dewangan, L. K., et al. 2015, MNRAS, 454, 4335
Bertoldi, F. 1989, ApJ, 346, 735
Bessell, M. S., & Brett, J. M. 1988, PASP, 100, 1134
Bisbas, T. G., Wünsch, R., Whitworth, A. P., & Hubber, D. A. 2009, A&A, 497, 649
Buckle, J. V., Hills, R. E., Smith, H., et al. 2009, MNRAS, 399, 1026
Cartwright, A., & Whitworth, A. P. 2004, MNRAS, 348, 589
Chauhan, N., Pandey, A. K., Ogura, K., et al. 2009, MNRAS, 396, 964
Chavarría, L., Allen, L., Brunt, C., et al. 2014, MNRAS, 439, 3719
Chrysostomou, A., Brand, P. W. J. L., Burton, M. G., & Moorhouse, A. 1992, MNRAS, 256, 528
Cohen, J. G., Frogel, J. A., Persson, S. E., & Elias, J. H. 1981, ApJ, 249, 481
Cooper, H. D. B., Lumsden, S. L., Oudmaijer, R. D., et al. 2013, MNRAS, 430, 1125
Cutri, R. M., Skrutskie, M. F., van Dyk, S., et al. 2003, 2MASS All Sky Catalog of Point Sources (Washington, DC: NASA/IPAC Infrared Science Archive)
Cutri, et al. 2014, yCat, 2328, 0
Dale, J. E., Bonnell, I. A., & Whitworth, A. P. 2007, MNRAS, 375, 1291
Deharveng, L., Schuller, F., Anderson, L. D., et al. 2010, A&A, 523, A6
Deharveng, L., Zavagno, A., & Caplan, J. 2005, A&A, 433, 565
Dewangan, L. K., Baug, T., Ojha, D. K., & Ghosh, S. K. 2018, ApJ, 869, 30
Dewangan, L. K., Luna, A., Ojha, D. K., et al. 2015, ApJ, 811, 79
Dewangan, L. K., Sano, H., Enokiya, R., et al. 2019, ApJ, 878, 26
Dobashi, K., Bernard, J.-P., Yonekura, Y., & Fukui, Y. 1994, ApJS, 95, 419
Downes, D., & Rinehart, R. 1966, ApJ, 144, 937
Duronea, N. U., Vasquez, J., Cappa, C. E., Corti, M., & Arnal, E. M. 2012, A&A, 537, A149
Dyson, J. E., & Williams, D. A. 1980, Physics of The Interstellar Medium (Manchester: University Press)
Elmegreen, B. G. 1998, in ASP Conf. Ser. 148, Observations and Theory of Dynamical Triggers for Star Formation, ed. C. E. Woodward et al. (San Francisco, CA: ASP), 150
Elmegreen, B. G., & Lada, C. J. 1977, ApJ, 214, 725
Flaherty, K. M., Pipher, J. L., Megeath, S. T., et al. 2007, ApJ, 663, 1069
Gaia Collaboration, Brown, A. G. A., Vallenari, A., et al. 2018, A&A, 616, A1
Girardi, L., Bertelli, G., Bressan, A., et al. 2002, A&A, 391, 195
Goicoechea, J. R., Cuadrado, S., Pety, J., et al. 2018, in IAU Symp. 332, Astrochemistry VII: Through the Cosmos from Galaxies to Planets, ed. M. Cunningham, T. Millar, & Y. Aikawa (Cambridge: Cambridge Univ. Press), 210
Gutermuth, R. A., Megeath, S. T., Myers, P. C., et al. 2009, ApJS, 184, 18
Henney, W. J., Arthur, S. J., & García-Díaz, M. T. 2005, ApJ, 627, 813
Hernández, J., Calvet, N., Hartmann, L., et al. 2005, AJ, 129, 856
Hosokawa, T., & Inutsuka, S.-I. 2006, ApJ, 646, 240
Hunter, D. A., & Massey, P. 1990, AJ, 99, 846
Israel, F. P. 1978, A&A, 70, 769
Jacoby, G. H., Hunter, D. A., & Christian, C. A. 1984, ApJS, 56, 257
Knödlseder, J. 2000, A&A, 360, 539
Koenig, X. P., & Leisawitz, D. T. 2014, ApJ, 791, 131
Kruijssen, J. M. D., Schruba, A., Chevance, M., et al. 2019, Natur, 569, 519
Krumholz, M. R., & Matzner, C. D. 2009, ApJ, 703, 1352
Kwan, J. 1997, ApJ, 489, 284
Lada, C. J., & Adams, F. C. 1992, ApJ, 393, 278
Lada, C. J., Lada, E. A., Clemens, D. P., & Bally, J. 1994, ApJ, 429, 694
Lahulla, J. F. 1985, A&ASS, 61, 537
Lawrence, A., Warren, S. J., Almaini, O., et al. 2007, MNRAS, 379, 1599
Lefloch, B., & Lazareff, B. 1994, A&A, 289, 559
Lefloch, B., & Lazareff, B. 1995, A&A, 301, 522
Lefloch, B., Lazareff, B., & Castets, A. 1997, A&A, 324, 249
Lucas, P. W., Hoare, M. G., Longmore, A., et al. 2008, MNRAS, 391, 136
Luri, X., Brown, A. G. A., Sarro, L. M., et al. 2018, A&A, 616, A9
Maheswar, G., Sharma, S., Biman, J. M., Pandey, A. K., & Bhatt, H. C. 2007, MNRAS, 379, 1237
Mallick, K. K., Kumar, M. S. N., Ojha, D. K., et al. 2013, ApJ, 779, 113
Mallick, K. K., Ojha, D. K., Samal, M. R., et al. 2012, ApJ, 759, 48
Martins, F., Schaerer, D., & Hillier, D. J. 2005, A&A, 436, 1049
Maud, L. T., Lumsden, S. L., Moore, T. J. T., et al. 2015a, MNRAS, 452, 637
Maud, L. T., Moore, T. J. T., Lumsden, S. L., et al. 2015b, MNRAS, 453, 645
Meyer, M. R., Calvet, N., & Hillenbrand, L. A. 1997, AJ, 114, 288
Meynet, G., Maeder, A., Schaller, G., Schaerer, D., & Charbonnel, C. 1994, A&ASS, 103, 97
Morgan, L. K., Thompson, M. A., Urquhart, J. S., White, G. J., & Miao, J. 2004, A&A, 426, 535
Motte, F., Bontemps, S., & Louvet, F. 2018, ARA&A, 56, 41
Ojha, D. K., Ghosh, S. K., Kulkarni, V. K., et al. 2004a, A&A, 415, 1039
Ojha, D. K., Tamura, M., Nakajima, Y., et al. 2004b, ApJ, 616, 1042
Omar, A., Chengalur, J. N., & Anish Roshi, D. 2002, A&A, 395, 227
Ortega, M. E., Paron, S., Giacani, E., Rubio, M., & Dubner, G. 2013, A&A, 556, A105
Paladini, R., Umana, G., Veneziani, M., et al. 2012, ApJ, 760, 149
Panagia, N. 1973, AJ, 78, 929
Pandey, R., Sharma, S., Panwar, N., et al. 2020, ApJ, 891, 81
Panwar, N., Chen, W. P., Pandey, A. K., et al. 2014, MNRAS, 443, 1614
Panwar, N., Samal, M. R., Pandey, A. K., et al. 2017, MNRAS, 468, 2684
Panwar, N., Samal, M. R., Pandey, A. K., Singh, H. P., & Sharma, S. 2019, AJ, 157, 112
Pellegrini, E. W., Oey, M. S., Winkler, P. F., et al. 2012, ApJ, 755, 40
Pomarès, M., Zavagno, A., Deharveng, L., et al. 2009, A&A, 494, 987
Samal, M. R., Pandey, A. K., Ojha, D. K., et al. 2007, ApJ, 671, 555
Schmeja, S., & Klessen, R. S. 2006, A&A, 449, 151
Schneider, N., Bontemps, S., Simon, R., et al. 2006, A&A, 458, 855
Sharma, S., Pandey, A. K., Borissova, J., et al. 2016, AJ, 151, 126
Sharma, S., Pandey, A. K., Ojha, D. K., et al. 2017, MNRAS, 467, 2943
Sharpless, S. 1959, ApJS, 4, 257
Siess, L., Dufour, E., & Forestini, M. 2000, A&A, 358, 593
Stalin, C. S., Hegde, M., Sahu, D. K., et al. 2008, BASI, 36, 111
Stone, R. P. S. 1977, ApJ, 218, 767
Tan, J. C., Beltrán, M. T., Caselli, P., et al. 2014, in Protostars and Planets VI, ed. H. Beuther et al. (Tucson, AZ: Univ. Arizona Press), 149
Taylor, A. R., Gibson, S. J., Peracaula, M., et al. 2003, AJ, 125, 3145
Tenorio-Tagle, G. 1979, A&A, 71, 59
Thompson, M. A., Urquhart, J. S., & White, G. J. 2004, A&A, 415, 627
Urquhart, J. S., Hoare, M. G., Purcell, C. R., et al. 2009, A&A, 501, 539
Urquhart, J. S., Morgan, L. K., Figura, C. C., et al. 2011, MNRAS, 418, 1689
Uyanıker, B., Fürst, E., Reich, W., Aschenbach, B., & Wielebinski, R. 2001, A&A, 371, 675
Vig, S., Ghosh, S. K., Ojha, D. K., Verma, R. P., & Tamura, M. 2014, MNRAS, 440, 3078
Walborn, N. R., & Fitzpatrick, E. L. 1990, PASP, 102, 379
Whitworth, A. P., Bhattal, A. S., Chapman, S. J., Disney, M. J., & Turner, J. A. 1994, A&A, 290, 421
Wright, E. L., Eisenhardt, P. R. M., Mainzer, A. K., et al. 2010, AJ, 140, 1868
Zavagno, A., Russeil, D., Motte, F., et al. 2010, A&A, 518, L81
Zinnecker, H., & Yorke, H. W. 2007, ARA&A, 45, 481